



# Effect of local stiffeners and warping constraints on the buckling of symmetric open thin-walled beams with high warping stiffness

G. Piana · E. Lofrano · A. Carpinteri · G. Ruta

Received: 20 December 2020 / Accepted: 30 March 2021 / Published online: 20 April 2021  
© The Author(s) 2021

**Abstract** Local stiffeners affect the behaviour of thin-walled beams (TWBs). An in-house code based on a one-dimensional model proved effective in several instances of compressive buckling of TWBs but gave counterintuitive results for locally stiffened TWBs. To clarify the matter, we investigated TWBs with multi-symmetric double I cross-section, widely used in practical applications where high bending stiffness is required. Several samples were manufactured and stiffened on purpose, closing them over a small portion of the axis at different places. The samples were tested with end constraints accounting

for various warping conditions. The experimental and numerical outputs from a commercial FEM code gave a key to overcome the unexpected results by the in-house code, paving the way for further studies.

**Keywords** Local stiffeners · Warping constraints · Open thin-walled beams · Torsion buckling

## 1 Introduction

Open thin-walled beams (TWBs) have high bending stiffness and negligible twisting stiffness; boundary effects propagate through their length (Saint–Venant’s principle does not apply [1]). The cross-sections warp; extension, bending and torsion are usually coupled. Thus, buckling strongly depends on their warping stiffness and on the constraints on torsion and warping. A comprehensive treatise is Vlasov’s well-known monograph [2]; starting from it, we may find innumerable papers and books dealing with the subject. For sake of space, we quote only those that are directly related with the experimental and numerical work in this contribution.

The authors recently investigated the compressive buckling of open thin-walled profiles by both numerical and experimental analysis. In [3–6] we describe the experimental campaigns to measure the variation of the natural frequencies and the buckling loads (for a description of the phenomenon see, e.g., [7–12]) of

---

G. Piana (✉) · A. Carpinteri  
Department of Structural, Geotechnical and Building  
Engineering, Turin Polytechnic, Turin, Italy  
e-mail: gianfranco.piana@polito.it

A. Carpinteri  
e-mail: alberto.carpinteri@polito.it

G. Piana  
Department of Bridge Engineering, Tongji University,  
Shanghai, People’s Republic of China

E. Lofrano · G. Ruta  
Department of Structural and Geotechnical Engineering,  
University “La Sapienza”, Rome, Italy  
e-mail: egidio.lofrano@uniroma1.it

G. Ruta  
e-mail: giuseppe.ruta@uniroma1.it

E. Lofrano · G. Ruta  
National Group for Mathematical Physics, Rome, Italy

compressed open thin-walled profiles. An experimental campaign similar to ours was recently presented in [13]. The profiles we investigated were manufactured in aluminium on purpose for the tests, had cross-sections once with vanishing, then with high warping stiffness. We also investigated open profiles without symmetry (thus, exhibiting strong couplings among deformation modes) and others with a small local damage.

The experimental results were positively compared with the numerical ones of the *in-house* centred finite differences code introduced in [14]. This relies on the direct one-dimensional beam model discussed in [15, 16]: the usual rigid cross-sections are added a coarse descriptor of warping, and non-linear coupled elastic relations are adopted. Thus, Vlasov's governing equations for open thin-walled profiles are recovered. The *in-house* code investigates elastic stability in a Lyapunov's dynamic setting [17] and is inspired by the numerical approach in [18]. The code accounts for the cross-section warping following [15, 16] and the constitutive coefficients are evaluated according to the beam model in [19], derived from that of a thin shell. There are many other analytical and numerical approaches to the subject (see, e.g., [20, 21]), but we chose a direct one-dimensional formulation for sake of simplicity and for the relative easiness with which results can be obtained and compared with experimental ones.

The results in [14] proved the *in-house* code to be effective, admitting usual constraints on bending and ideal constraints on warping. However, the effect of the conditions on the torsion rotation and warping of the end cross-sections propagates through the beam and affects both the natural frequencies and the buckling loads [1, 2]. Thus, in order to perform a thorough investigation and provide 'actual' data to insert into the *in-house* code, suitable end constraints for laboratory tests were designed and manufactured in brass. These devices were thus subsequently simulated by suitable analytical and numerical boundary conditions. The results of all the experimental and numerical investigations showed good agreement and were reported in our previous works [3–6]. This highlighted that the *in-house* code is both robust and simple, basing on a well-tested one-dimensional model, which quickly and effectively brings reliable results that can be useful in design and verification of TWBs.

However, counterintuitive results arose when we evaluated the buckling loads of TWBs with local stiffeners, which are widely used in engineering. Indeed, in many applications the modest torsion rigidity of open TWBs asks for interventions to limit the corresponding shearing stress and cross-sections warping. Hence, actual assemblies of thin-walled open profiles may exhibit local stiffeners, e.g., transverse plates or reinforcing frames. These are located at specific points, to limit the in-plane deformations of the cross-sections and/or to protect the element, hence the whole structure, against local buckling [22–26]. When we ran our *in-house* code to evaluate such effects, introducing the modified cross-section properties of the reinforced zones, we found the surprising result that for some locations of the stiffeners the buckling load was *lower* than for the corresponding unstiffened profile. Some of these unexpected results, published in congress proceedings [27], asked for deeper investigations to clarify the behaviour of the one-dimensional model and its numerical implementation.

Thus, here we perform alternative numerical analyses and experimental tests: the investigated profiles have double I (cruciform) cross-sections. Despite this easiness, such profiles are suitable for the analysis since they are: (a) used in real-life applications; (b) stiff remarkably in bending and non-negligibly in warping. The surprising results by the *in-house* code are evidenced, thoroughly discussed and overcome by a careful analysis of the other numerical and experimental results, plus a comparison with the existing literature on stiffened profiles. Thus, further following investigation seems necessary: the code, otherwise reliable, leans on simplifying assumptions on kinematics and constraints, hence a deeper insight on the modelling and numerical aspects needs to be performed in the next future and is already scheduled.

The paper is organised as follows: Sect. 2 describes the specimens used, specifies their geometrical and material characteristics, plus the realisation of the stiffeners, which are simple and require a very low amount of material and work. Then, we numerically investigate how the intermediate stiffeners affect the buckling loads of the profiles when these are compressed. Similar to our previous works, two analyses are performed and presented in detail: one relies on commercial finite elements, Sect. 3, the other on *in-house* finite differences, Sect. 4. In Sect. 5 we describe

the laboratory setting for the experimental campaign and present the results of the tests on various specimens. The three sets of results are compared and duly commented, aiming to possible directions in design. The TWBs cross-sections are gyroscopic (i.e., any centroidal axis in the cross-section plane is a principal axis of inertia: second moments of area always have the same value and the product moment of area is always nil for any centroidal couple of orthogonal axes; in short, any definition for the inertia tensor returns a spherical one) but their usual application sees the webs parallel to the axes of a Cartesian plane frame. Since we study torsion buckling, and twist occurs with respect to the centroidal axis, the gyroscopic feature of the cross-sections is immaterial on the results and conclusions, reported in Sect. 6.

## 2 A set of TWBS with intermediate stiffeners

To simplify investigation, we choose aluminium open thin-walled profiles with (at least) doubly symmetric cross-sections. Indeed, to perform experiments by the MTS universal machines at ease in Turin Polytechnic, “soft” element shall be considered (otherwise, their lengths would be excessive); moreover, all the coupling terms in the constitutive laws for the profile identically vanish [15, 16, 19]. Thus, the governing equations are much simpler than those for elements with generic cross-sections and the dominant behaviour is in torsion or bending only, making both numerical analysis and laboratory activities easier to perform.

The chosen cross-section is a double I, with the contour and characteristic lengths shown in Fig. 1a. This shape was already considered by the authors in [3, 4, 6] to highlight the effect of a remarkable warping rigidity in the modulated linear dynamics and the buckling of open thin-walled beams. The specimens are made of the aluminium alloy known as 6060-T5.

The stiffening is obtained by closing the initial open shape of the cross-section, adding the small amount of material dashed in Fig. 1b (similar to what is done in [22–26]). We so realise a reinforcing frame of plates, as thick as the external flanges of the cross-section and connecting them so to yield a four-cell box. Multi-cell boxes are endowed with a very high rigidity to bending and torsion, thus are suitable for our analysis. We

remark that this operation requires little material and no particular additional manufacturing.

The numerical analysis requires length  $l$ , Young’s modulus  $E$ , Poisson’s ratio  $\nu$  (whence the shear modulus  $G = E/[2(1 + \nu)]$ ), material mass density per unit volume  $\rho$ , listed in Table 1. The material yield stress (used in Sect. 5.2 to check inelastic effects on experiments) is 120 MPa.

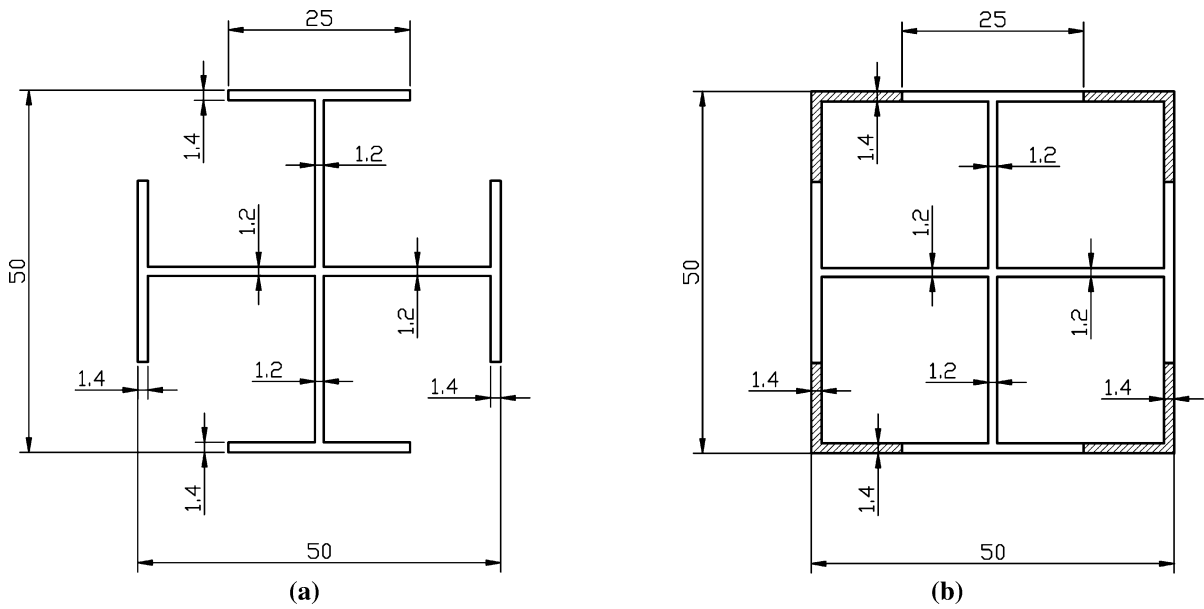
We adopt a Cartesian system  $\{O, x_1, x_2, x_3\}$ , with  $x_1$  the abscissa along the axis,  $O$  the centroid and  $x_2, x_3$  along the mid-lines of the cross-section webs. Table 2 lists the cross-section properties ( $i, j = 2, 3$ ): the area  $A$ ; the shear areas  $A_{ij}$  (accounting for the relevant shear factors); Saint–Venant’s torsion factor  $J$ ; the polar moment of inertia  $I_c$  with respect to the shear centre  $c$  (with coordinates  $x_{cj}$ ; for symmetric thin-walled cross-sections, Trefftz and Timoshenko definitions for  $c$  coincide [28]); the central principal moments of inertia  $I_j$ ; the flexure-torsion constitutive coupling constants  $I_{fj}$  [15, 16, 19]; and the warping constant  $\Gamma$  [1, 2]. Since the cross-sections are gyroscopic, all the couplings vanish, i.e.,  $A_{ij} = x_{cj} = I_{fj} = 0$ .

Table 2 also shows the percentage variation of cross-section properties. The area and shear areas increase, the flexural stiffness more than doubles; indeed, adding material far from the centroid = shear centre affects the latter more than the former. However, the torsion properties change significantly from an open profile to a closed multi-cell: Saint–Venant’s torsion factor grows by three orders of magnitude, the polar moment of inertia more than doubles (consistently with the moments of inertia), but the warping constant vanishes.

In our investigation, the stiffened portion of the profile has finite length, equal to one tenth of that of the specimen, see Fig. 2. Several samples manufactured by a company specialised in precision mechanics were purchased; details are in Sect. 5.

The stiffener acts as a diffused constraint against torsion rotation for a finite length and affects the transmission of warping (which is proportional to the unit torsion rotation, or twist) [1, 2, 15]. Then, one might wonder if such a diffused constraint is consistent with the vanishing warping stiffness in Table 2: the question will emerge strongly in the sequel.

We examine the effect of the stiffeners on the torsion buckling of the specimens under axial compression, presenting the results of numerical studies first, then those of experiments.



**Fig. 1** a Current and b stiffened cross-sections (dimensions in mm); dashed parts highlight the stiffener

**Table 1** Specimens’ axis length and material properties

$l$ (mm)	$E$ (N m <sup>-2</sup> )	$\nu$ (-)	$\rho$ (kg m <sup>-3</sup> )
950	$69 \times 10^9$	0.3	2600

### 3 Numerical investigations—finite elements

Dealing with TWBs, the specimens were meshed by shell elements in the commercial code LUSAS [29]. Linear buckling analyses were run for various end warping constraint conditions and stiffener locations,

**Table 2** Geometrical properties of the current and stiffened cross-sections

Cross-section	$A$ (mm <sup>2</sup> )	$A_{22} = A_{33}$ (mm <sup>2</sup> )	$A_{23} = A_{32}$ (mm <sup>2</sup> )	$J$ (mm <sup>4</sup> )	$I_c$ (mm <sup>4</sup> )	$I_2 = I_3$ (mm <sup>4</sup> )	$x_{c2} = x_{c3}$ (mm)	$I_{J2} = I_{J3}$ (mm <sup>5</sup> )	$\Gamma$ (mm <sup>6</sup> )
Current	251.84	110.38	0	148.36	111,028	55,514	0	0	4,305,656
Stiffened	384.00	200.02	0	163,945	235,498	117,749	0	0	0
Diff. (%)	52.5	81.2	-	110,405	112.1	112.1	-	-	- 100

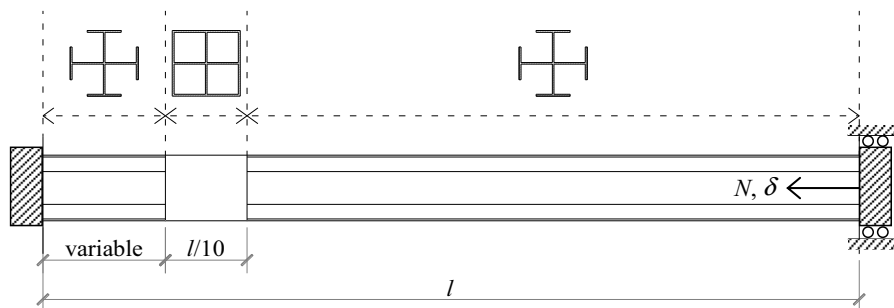


**Fig. 2** Sketch of the numerical and experimental tests;  $N, \delta$  are the axial force and the corresponding displacement

in number greater than experimental tests; the latter are described in Sect. 5. In all cases, bending and twist rotations were prevented at the ends. As for the warping constraints, the following cases were analysed: (a) warping free at both ends; (b) warping restrained at both ends; and (c) warping free at one end and restrained at the other. A single intermediate stiffener with length equal to one tenth of that of the beam was considered located at the following positions, relative to one end of the beam: 0– $l/10$ ;  $l/10$ – $2l/10$ ;  $2l/10$ – $3l/10$ ;  $4l/10$ – $5l/10$ ;  $4.5l/10$ – $5.5l/10$  (centred at mid-length). Cases with two intermediate stiffeners, placed symmetrically with respect to mid-length, were also analysed considering the following positions relative to the beam ends: 0– $l/10$ ;  $l/10$ – $2l/10$ ;  $2l/10$ – $3l/10$ ;  $3l/10$ – $4l/10$ .

After a preliminary convergence study, the beams were meshed by QSL8 thin shell elements, i.e., 8-nodes quadrilateral semi-loof elements with no transverse shearing strain, 3 d.o.f. in translation at corner nodes and 5 d.o.f. (3 in translation and 2 loof rotations) at mid-side nodes [29]. This mesh had 48 subdivisions along the open (current) cross-section, 80 along the closed (stiffened) cross-section, and 304 subdivisions in the longitudinal direction (30 of which relative to the stiffened part), yielding 15'552 shell elements in total. The properties of the material, assumed linearly elastic and isotropic, were set according to the values in Table 1.

Aiming to match the experimental conditions (see Sect. 5.1), end constraints were applied to either the cruciform web only or to the whole cross-section, for free (Fig. 3) and restrained warping (Fig. 4),

respectively. Thus, all node translation and rotation components were prevented, except for the axial displacement (in the Z-direction) of the top section, where a unit compressive axial force was applied to the centroid (Figs. 3a and 4a). For restrained warping, to prevent it at the top section but allowing for axial translation at the same time, a 1 mm thick layer of material with high stiffness (Young's modulus  $E = 10^{15}$  Pa) was introduced (Fig. 4a), so that the relevant cross-section remains plane but may translate along the axis of the profile.

Figure 5 shows the numerical model and the first buckling mode of a specimen stiffened before midspan, i.e., between  $4l/10$ – $5l/10$  (380–475 mm); warping is free at both ends. The first buckling mode is in torsion: the beam axis twists but remains straight. This behaviour is fairly usual for open TWBs of moderate length (otherwise, flexural buckling prevails) and cruciform sections with and without flanges. Please remark that the stiffened part apparently does not twist, in accord with the mechanical role of the introduced reinforcement. The buckling load, equal to 17.7 kN for the unstiffened profile with the same end constraints (16.5 kN if the end constraints act only at the centroid, not on the whole web) [6], grows to 18.79 kN. The analytic solution for torsion buckling of TWBs [1, 12] gives the buckling load of 16.3 kN for the unstiffened profile [6], a value close to the mentioned numerical counterpart of 16.5 kN.

Figure 6 shows a contour plot of the axial displacements (DZ) in the same buckling mode of Fig. 5. As it is well known, the eigenvector has undefined amplitude; thus, we do not read actual displacements but

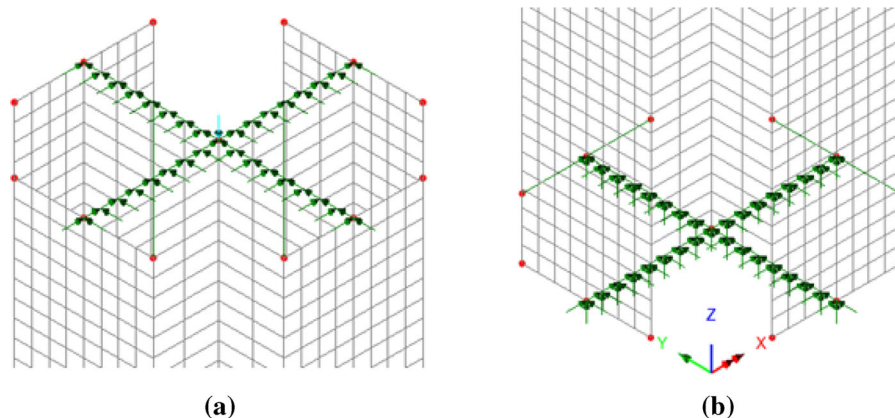
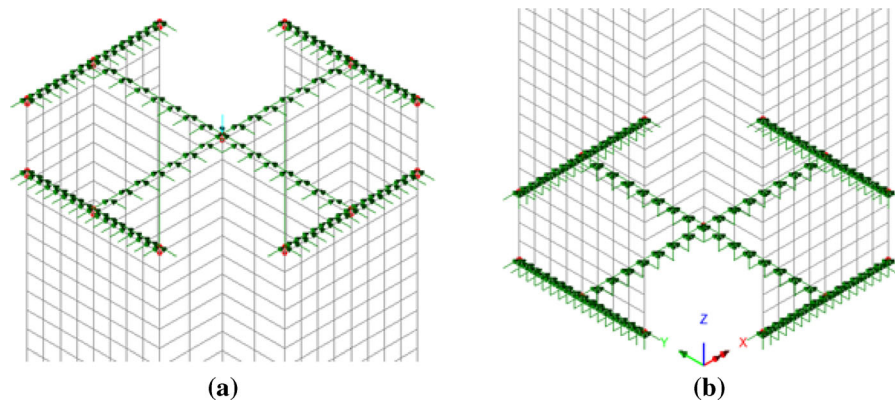
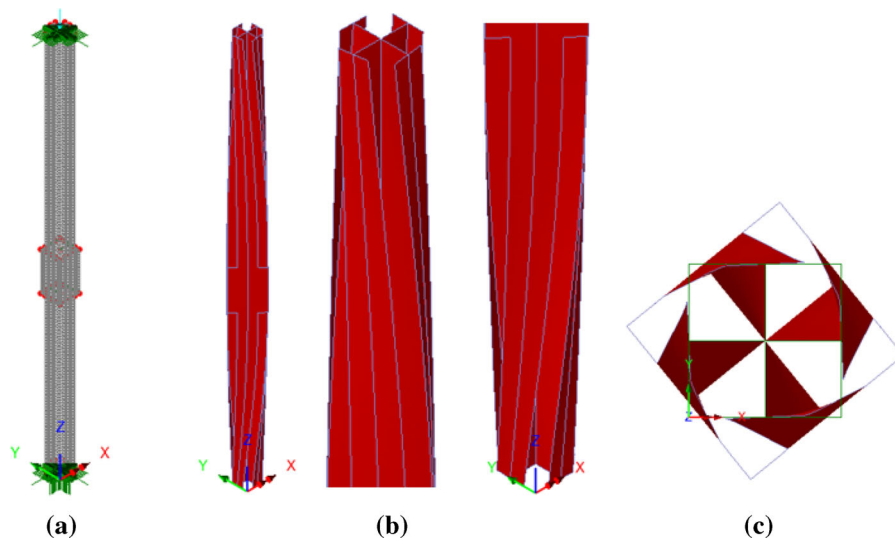


Fig. 3 Detail of the mesh and end restraints for free warping at a top and b bottom ends



**Fig. 4** Detail of the mesh and end restraints for restrained warping at **a** top and **b** bottom ends

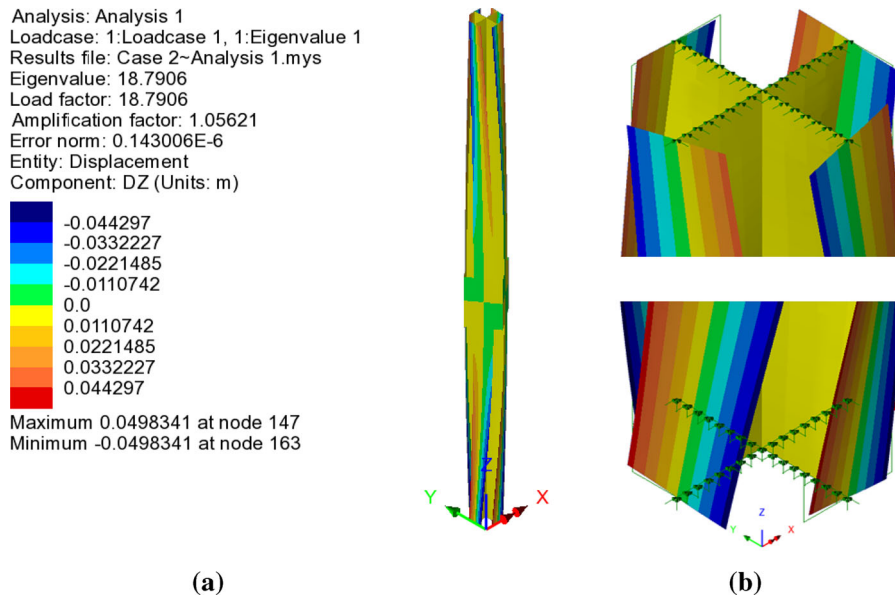


**Fig. 5** Stiffener at  $4 l/10$ – $5 l/10$ , free warping at the ends (case 2 of Table 3): **a** FEM model; **b** lateral and **c** top view of the first buckling mode

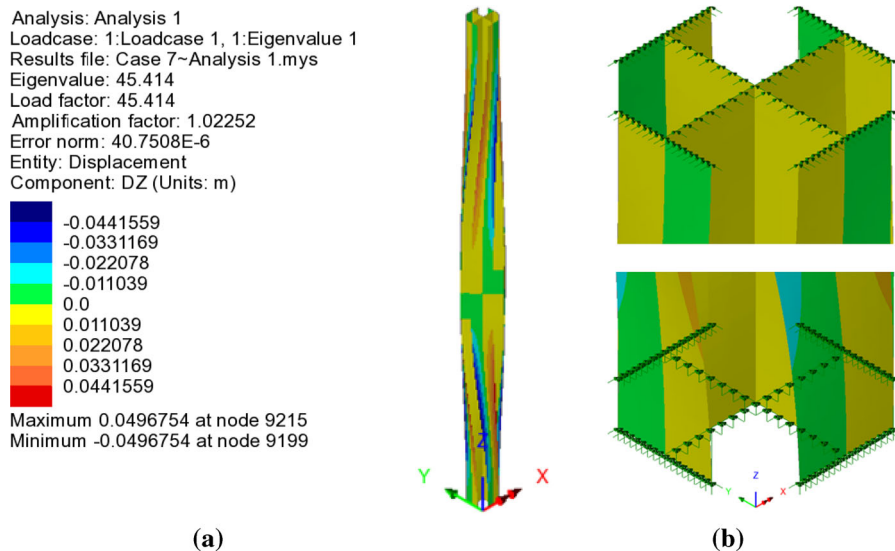
simply have a visual sketch for the cross-section warping and the stiffener effect. Red and blue denote extrema of axial displacements, of equal magnitude and opposite direction. A transition to yellow and green indicates that their absolute value decreases until zero. As expected, the largest cross-section warping is at the ends, then it gradually vanishes in approaching the stiffener, Fig. 6a, thus confirming its effect on warping also. Figure 6b shows also a detail of the end cross-sections: each flange warps out of its plane by axial displacements that linearly decreases from the ends and vanish at the mid-point. There, the flanges connect with the web, which does not warp; both features follow the TWBs theory [2].

Figure 7 shows the first buckling mode of the same profile considered in Figs. 5 and 6 when warping is prevented at both ends. As before, buckling is in torsion, but the corresponding load increases to 45.41 kN. The relevant unstiffened profile buckles at 38.4 kN, according to both shell FE model and TWB analytic formula [6]. From Fig. 7b, we clearly see that warping vanishes at the ends and in the stiffened zone, confirming the previous remarks.

Table 3 lists the elastic buckling loads ( $N_{b,e}$ ) given by FEM. For both free and restrained end warping conditions, we can identify the best location of the stiffener(s) to maximise the buckling load. One stiffener should lie in the interval  $2 l/10$ – $3 l/10$ ,



**Fig. 6** First buckling mode as in Fig. 5: **a** contour plot of axial displacements (DZ); **b** warping of the ends



**Fig. 7** First buckling mode for the same stiffened beam as in Fig. 5, but with end warping restrained: **a** contour plot of axial displacements (DZ); **b** no warping of the ends

independent of the end warping restraints (cases 3, 8). Two symmetrically placed stiffeners have best location in the interval:  $l/10-2l/10$ , if end warping is free (case 20);  $2l/10-3l/10$ , if it is restrained (case 23). By comparing the different warping constraint conditions and stiffened configurations, we infer that the considered stiffener acts as a full inner warping constraint, the effects of which propagate along the beam length.

Indeed, among the analysed configurations, we get the same buckling loads in cases 4–14, 5–16, 9–15, 10–17, 20–24–26, and 21–25–27. The elastic buckling stress  $\sigma_{b,e} = N_{b,e}/A$  is compared in Sect. 5 with the yield stress of the specimens' material, so to evaluate the elastic-plastic buckling loads and compare them with the experimental critical ones.

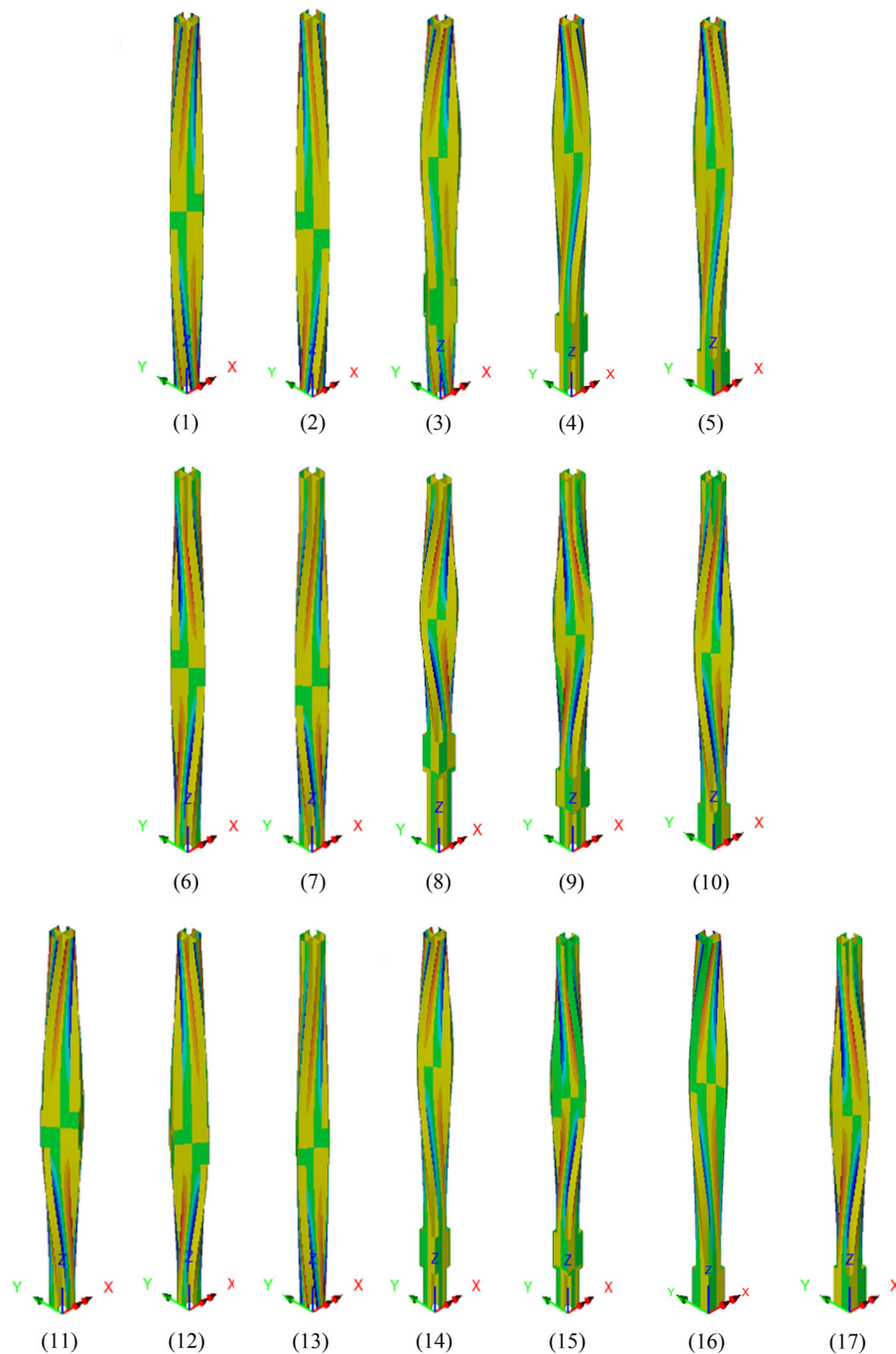


**Fig. 8** Contour plot of the axial displacements (DZ), first buckling mode of the beams with one stiffener in Table 3, with warping: (1–5) free-free; (2–10) restrained-restrained; (11–17) free-restrained or vice versa

Figures 8 and 9 show the contour plots of the first buckling modes for all the beams in Table 3, reinforced by one or two stiffeners. The plot of the longitudinal displacements (denoted DZ again) is

superposed to the buckled shape, thus helping to understand the effect of the stiffening in relation to the results in Table 3. We remark that the walls length-to-thickness ratio is such that no apparent local nor



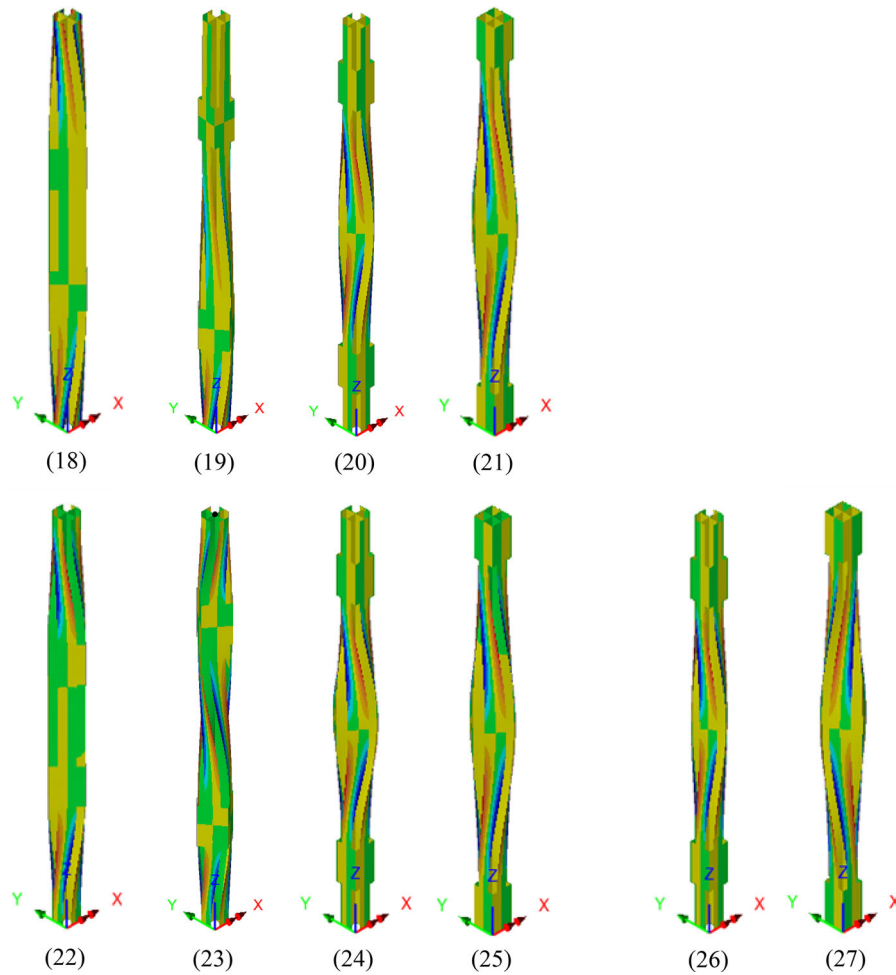


**Fig. 9** Contour plot of the axial displacements (DZ), first buckling mode of the beams with two stiffeners in Table 3, with warping: (18–21) free-free; (22–25) restrained-restrained; (26–27) free-restrained or vice versa

distortional buckling [30] takes place; this was also confirmed by the experiments, except only small regions near the ends in the case of restrained warping.

#### 4 Numerical investigations—finite differences

The *in-house* code used in this section was originally proposed by some of the authors in [14] and is based on a one-dimensional model for thin-walled beams with finite kinematics; balance is obtained equating external and internal powers. Non-linear hyper-elastic constitutive laws consider the coupling between extension and bending; extension, torsion and warping; shear forces; shear and torsion; bending and torsion. In few words, the model is a non-linear

Timoshenko-like beam endowed with a coarse scalar descriptor of warping, postulated to be proportional to the twisting couple; loadings can be either conservative or not.

The solution strategy in the code relies on a centred finite difference scheme (FDM) able to describe static equilibria; in detail, the Levenberg–Marquardt method was chosen to solve the system of non-linear equations. A ‘small’ perturbation superimposed on equilibrium leads to an eigenvalue problem and Lyapunov stability is studied, providing static and dynamic bifurcations (buckling and flutter). For the sake of brevity, the full set of governing equations and its finite differences implementation are not shown here; interested readers may refer to [14].

The code proved to be robust and reliable, since it was validated through several numerical and experimental investigations. Indeed, in [3, 5, 6, 14] numerous case studies were proposed, for symmetric and non-symmetric cross-sections, considering both prominent and evanescent values of the warping rigidity. The code also proved to be capable of describing the effect of ‘follower’ non-conservative loads [31], the incidence of local weakening [4] and the non-linear behaviour of thin-walled open profiles undergoing large displacements [32].

The profiles numerically investigated in this section are those described in Sect. 2, see Table 1 and Fig. 2; their cross-sections are those indicated by Table 2 and Fig. 1. In detail, following the FEM analysis in Sect. 3, we selected the cases 1 to 10 of Table 3. To sum up, these refer to a single stiffener with length one tenth of that of the beam,  $l$ ; its ends are placed at the following distance from the closest beam end:  $4.5 // 10$ – $5.5 // 10$ ,  $4 // 10$ – $5 // 10$ ,  $2 // 10$ – $3 // 10$ ,  $// 10$ – $2 // 10$ ,  $0 // 10$ . Boundary conditions prevent all displacements and rotations; an axial displacement is imposed at one end, whereas warping is free in cases 1–5, and restrained in cases 6–10. The cases 11–27 investigated in Sect. 3, about non-symmetric constraint conditions and/or two stiffeners, are not considered here: indeed, the simulations for the cases 1–10 suffice to express an opinion on the capabilities of the code. On the other hand, in addition to the cases 1–10 of Table 3, other five cases are introduced, denoted  $6^*$ ,  $7^*$ ,  $8^*$ ,  $9^*$  and  $10^*$ , respectively. They basically equal the cases 6, 7, 8, 9, 10, but the warping stiffness  $\Gamma$  is posed half the values in Table 2. The authors used this numerical artifact successfully in other studies, e.g., [6], aiming to model a semi-restrained warping, and intended to match the experimental conditions of joint devices able to prevent penetration, but not detachment of the beam ends. In other words, these non-linear constraints are simulated in the code by assuming that the beam ends are fully restrained against warping but considering half the actual warping stiffness.

The fifteen simulations are run considering 50 chunks along the beam; the length of each chunk is uniform and equal to 19 mm. This large number of elements satisfies the result of a preliminary convergence analysis and aims to accurately represent the structural response of all the case studies. Since the length of the stiffeners is one tenth of that of the beam, a sequence of 5 chunks models a stiffener. Remark that

the location of this sequence varies along the beam to cover the actual placement, Fig. 2, and that these five chunks have the sectional properties of the stiffened cross-section (whereas all the others have the initial ones, Table 2). We stress that, once the field equations have been discretised in the FD framework ([14]), a suitable updating of the geometrical properties of the considered chunks suffices to describe variations of the cross-section along the beam axis.







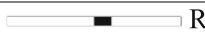
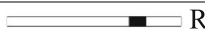






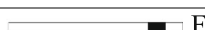












Analogously to the FEM results in Table 3, Table 4 compares these buckling loads with those provided by the *in-house* FDM-based code. In detail, the values of the fourth column, referring to the FEM analysis, are the same already listed in Table 3. However, the semi-restrained cases (cases  $6^*$  to  $10^*$ ) were not considered by FEM because the numerical artifice used to simulate this boundary condition cannot be used with models other than one-dimensional ones.

By analysing the results of the FDM code only (fifth column of Table 4), it is manifest how the warping constraint at the ends of the considered profile strongly affects its buckling load. In fact, when comparing the cases where the sample presents a stiffening located at the same position (i.e., case 1 versus case 6, case 2 versus case 7, and so on), we see that the critical loads have at least doubled when passing from free to restrained warping constraints at the ends of the profile. When semi-restrained warping is considered, we get values of the buckling loads that are intermediate between those for free and fully restrained warping at the ends of the profile. It is worth remarking that this is expected, being consistent with the physics of the problem.

However, comparing the FEM and FDM outcomes, large discrepancies turn out (4th and 5th columns of Table 4). Indeed, the critical loads provided by the FDM are always smaller than the FEM counterparts, with high percentage reductions (6th column of Table 4), ranging from 9 to 68%. That is, an otherwise robust and reliable numerical code that was effective in numerous cases of interest and was validated by several experimental tests (as well as numerical solutions, when available), provides unexpected results when stiffeners are considered.

To find the reasons behind these high differences, it is useful to compare the results by FEM and FDM, considering the same profiles of Table 4 with the same end constraints, now unstiffened. Therefore, only three cases survive, differing for the ends warping

**Table 3** FEM elastic buckling loads and corresponding pressures for different stiffener(s) positions and end warping constraints (F = free warping, R = restrained warping)









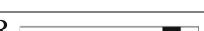






Case n.	Stiffened beam	Stiffener position from closest end	Elastic buckling load $N_{b,e}$ (kN)	Elastic buckling pressure $\sigma_{b,e}$ (MPa)
1	F  F	4.5l/10–5.5l/10	18.34	72.82
2	F  F	4l/10–5l/10	18.79	74.61
3	F  F	2l/10–3l/10	39.20	155.65
4	F  F	l/10–2l/10	33.90	134.61
5	F  F	0–l/10	28.67	113.84
6	R  R	4.5l/10–5.5l/10	43.34	172.09
7	R  R	4l/10–5l/10	45.41	180.31
8	R  R	2l/10–3l/10	66.35	263.46
9	R  R	l/10–2l/10	53.21	211.28
10	R  R	0–l/10	44.10	175.11
11	F (R)  R (F)	4.5l/10–5.5l/10	31.60	125.48
12	F  R	4l/10–5l/10	36.93	146.64
13	R  F	4l/10–5l/10	27.00	107.21
14	F  R	l/10–2l/10	33.90	134.61
15	R  F	l/10–2l/10	53.21	211.28
16	F  R	0–l/10	28.67	113.84
17	R  F	0–l/10	44.10	175.11
18	F  F	3l/10–4l/10	30.07	119.40
19	F  F	2l/10–3l/10	52.04	206.64
20	F  F	l/10–2l/10	84.26	334.58
21	F  F	0–l/10	52.35	207.87
22	R  R	3l/10–4l/10	83.94	333.31
23	R  R	2l/10–3l/10	108.78	431.94
24	R  R	l/10–2l/10	84.26	334.58
25	R  R	0–l/10	52.35	207.87
26	F (R)  R (F)	l/10–2l/10	84.26	334.58
27	F (R)  R (F)	0–l/10	52.35	207.87

conditions; the results are in Table 5. Firstly, the numerical data still reveal the significance of the warping constraint at the ends of the beam. Secondly, we note how this time the percentage differences among the two sets of results are very small, less than 1% in absolute value.

Basically, the comparisons in Table 5 indicate that the two codes begin to exhibit different behaviours

only when stiffeners are introduced. However, the most surprising outcome raised from Table 5 comes when comparing the values of the buckling load for unstiffened beams (Table 5) with those of the same beams when stiffened (Table 4). Indeed, the FDM code seems to indicate a counterintuitive behaviour in which the presence of the stiffener can, for some placements, reduce the critical load of the

**Table 4** FEM versus FDM elastic buckling loads for different stiffener positions and end warping constraints (F = free warping, R = restrained warping, S = semi-restrained warping)

Case n.	Stiffened beam	Stiffener position from closest beam end	Elastic buckling load- FEM $N_{b,e}$ (kN)	Elastic buckling load- FDM $N_{b,e}$ (kN)	Diff., %
1	F  F	4.5l/10–5.5l/10	18.34	8.95	– 51
2	F  F	4l/10–5l/10	18.79	9.05	– 52
3	F  F	2l/10–3l/10	39.20	12.45	– 68
4	F  F	l/10–2l/10	33.90	16.35	– 52
5	F  F	0–l/10	28.67	18.05	– 37
6	R  R	4.5l/10–5.5l/10	43.34	18.05	– 58
7	R  R	4l/10–5l/10	45.41	18.85	– 58
8	R  R	2l/10–3l/10	66.35	38.65	– 42
9	R  R	l/10–2l/10	53.21	42.05	– 21
10	R  R	0–l/10	44.10	40.25	– 9
6*	S  S	4.5l/10–5.5l/10	–	13.45	–
7*	S  S	4l/10–5l/10	–	13.85	–
8*	S  S	2l/10–3l/10	–	23.85	–
9*	S  S	l/10–2l/10	–	26.15	–
10*	S  S	0–l/10	–	25.75	–

**Table 5** FEM versus FDM elastic buckling loads for prismatic beams with different end warping constraints (F = free warping, R = restrained warping, S = semi-restrained warping)

Warping constraints	Elastic buckling load FEM, $N_{b,e}$ (kN)	Elastic buckling load FDM, $N_{b,e}$ (kN)	Differences (%)
F–F	16.50	16.35	– 0.9
R–R	38.40	38.45	0.1
S–S	–	23.75	–

No stiffeners are considered

corresponding unstiffened beam (see [27]). This surprising result occurs for seven of the fifteen case studies, viz. n. 1, 2, 3, 6, 7, 6\*, and 7\*.

On the one hand, since the code was already widely validated in many contributions in the last seven years [3, 5, 6, 14], even for non-prismatic beams [4] and strong non-linearities [32], code bugs can be excluded. On the other hand, the FEM results and physical intuition seem to suggest that the key point is how the stiffening portion is described in the one-dimensional beam model (hence, in the numerical code relying on

it). Indeed, as it was pointed out previously, it is strange that a reinforced chunk is characterised by a vanishing stiffness whatsoever. In short, the coarse description of the constitutive properties of the 1-D model looks unsuitable to describe an abrupt transition from unstiffened to stiffened chunk. To overcome this drawback, intuition suggests that a stiffening portion may be modelled as an inner constraint towards warping: actually, this is also what one sees from the outputs of FEM in Figs. 8 and 9.

**Table 6** FDM with increased warping stiffness versus FEM elastic buckling loads for cases 1, 3 and 6

Case n.	Elastic buckling load, FDM versus FEM, $N_{b,e}$ (kN)								FEM
	FDM, $\Gamma_s$								
	0	$10^0 \Gamma_c$	$10^1 \Gamma_c$	$10^2 \Gamma_c$	$10^3 \Gamma_c$	$10^4 \Gamma_c$	$10^5 \Gamma_c$	$10^6 \Gamma_c$	
1	8.95	17.75	17.95	18.05	18.05	18.05	18.05	18.05	18.34
3	12.45	36.65	37.45	37.55	37.65	37.65	37.65	37.65	39.20
6	18.05	44.15	45.15	45.45	45.55	45.55	45.55	45.55	43.34

Thus, we disregarded the theoretical values for the warping constant  $I$  in Table 2 and considered that the stiffening portion acts so to increase them. In detail, we consider the values  $\Gamma_s$  of the stiffened portion equal to those of the unstiffened chunks,  $\Gamma_c$ , amplified by increasing orders of magnitude. The results of the FDM analysis, once these data are used, are in Table 6.

Consider the cases 1, 3, 6 of Tables 3 and 4: in cases 1 and 6 the FDM provides the lowest buckling loads for free and restrained end warping constraints, respectively, whereas case 3 is analysed to check the validity of the procedure for a non-symmetric element. Table 6 explicitly shows that turning the stiffened part into an effective warping constraint properly recovers the FEM results. That is, our intuition is confirmed, and the *in-house* code shows reliable again.

These findings, however, pose very interesting questions in both modelling and numerical rendering, since a ‘naïve’ application of the one-dimensional model might apparently yield wrong results. A problem similar to that emerged here applying the *in-house* FDM code could arise when using refined 1-D (i.e., beam) finite elements including cross-section warping due to torsion. This is hence worthy of further theoretical and computational investigation.

## 5 Experimental investigations and comparisons

### 5.1 Experimental set-up

Axial compression tests were made on an MTS universal machine with maximum loading capacity of 100 kN. The loading was displacement-controlled: the input was a monotonic increase of one axial end displacement, imposed by the linear actuator (hydraulic jack) at a speed 10  $\mu\text{m/s}$ ; the output was the axial load measured by the machine as a reactive force.

Figure 10a shows the experimental set-up: the specimen is held vertical by two brass end constraints, connected to the MTS by steel devices. The top end is connected to the fixed crossbar, while the lower end is fixed to the actuator by an element allowing horizontal adjustment during positioning (this was essential to ensure specimen verticality). Figure 10b shows a closest view of the stiffener (realised by welding angular plates to the flanges) and of the optoNCDT 1302–20 laser displacement transducer by Micro-Epsilon (Fig. 10b), mounted to monitor the transverse displacement of a control point located approximately at mid-length of the sample (Fig. 10a). The main features of such non-contact sensor are in Table 7. The measured transverse displacement was an indirect indicator of twist.

Figures 11a, b show the end constraints for free and prevented end warping, respectively; end displacements, rotations and twist are all prevented in both cases. The brass joints, available from previous studies of ours [3, 4, 6], were realised on purpose to fit the peculiar cross-section.

As discussed in the previous section, in the case of Fig. 11b the end warping of the flanges is only partially restrained, since the joints prevent penetration but not detachment of the terminal cross-sections: this can, on average, reasonably be assimilated to a half-restrained warping condition [6]. This circumstance must be considered when comparing experimental and numerical results. Even the geometrical imperfections and the residual stresses induced by welding of the stiffening plates were not taken into account in the numerical simulations but may have some importance for real prototypes. Despite the mentioned differences, a comparison between numerical predictions and experimental results is of primary interest, if only to check if the former is conservative, thus of possible use for engineering applications.

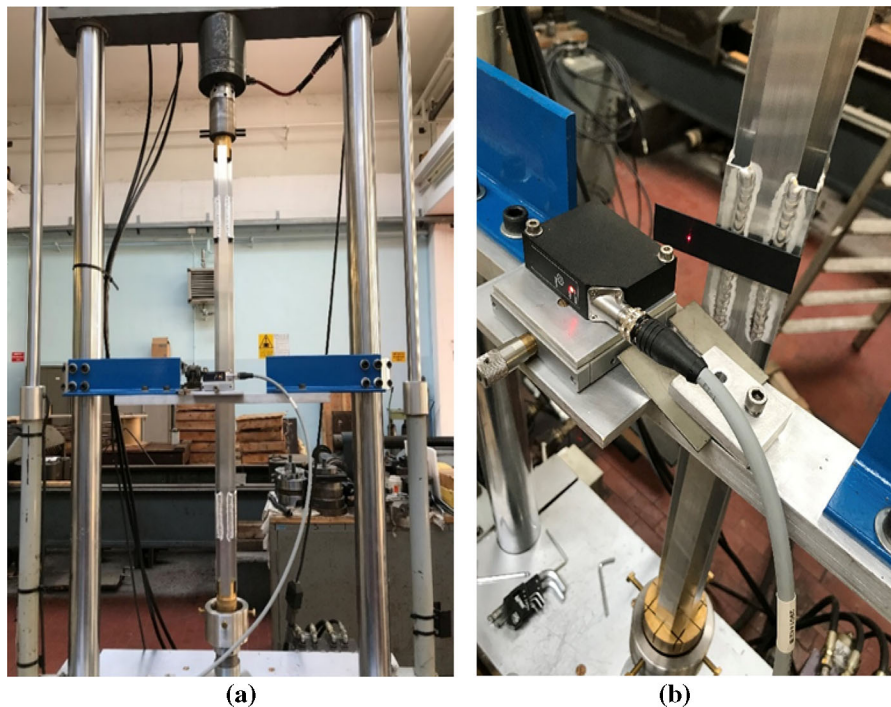


**Fig. 10** **a** Experimental set-up for axial compression; **b** particular of laser sensor and stiffening frame

**Table 7** Main features of the laser sensor

Measure range	Start of measure range	End of measure range	Linearity	Resolution
20 mm	30 mm	50 mm	40 $\mu\text{m}$	4 $\mu\text{m}$ (averaged) 10 $\mu\text{m}$ (dynamic 750 Hz)

An NI9215 device by National Instruments gave analogic to digital signal conversion. Data acquisition and analysis were performed by self-built LabVIEW programs. Two sets of curves emerged: axial load versus axial displacement and axial load versus twist rotation of the mid-span; they were used in a complementary way to evaluate the buckling load (see following section).

## 5.2 Experimental results and comparisons in elastic-plastic range

Referring to Table 3, the following nine cases were experimentally tested: 1, 2, 4, 5, 6, 7, 9, 21 and 24. Two tests were performed in cases 2, 6 and 7, while only one for the remaining cases, for a total of twelve tests. In detail: cases 1, 2, 4 and 5 have a single stiffener and free warping end conditions; 6, 7 and 9

have one stiffener and restrained end warping; 21 and 24 have two symmetric stiffeners, with free and restrained end warping, respectively (see Table 3). Tests were repeated once in three cases over nine (one case for free end warping, two cases for restrained end warping), showing a good match in terms of buckling load, limit load, and slope of the axial load versus axial displacement curve (see Figs. 12 and 13). For this reason, although the limited number of tested specimens do not allow us to do any statistics for the analysed cases, we feel sufficiently confident about the general repeatability of the results.

Figures 12a, 13a and 14a show the axial load versus axial displacement plots for all the tested cases. All the curves show a similar qualitative trend, where three stages can be recognised: (1) a first phase characterised by a stiffening branch due to initial adjustments (to cover gaps within both end joints and the relevant



**Fig. 11** Top and bottom end constraints for **a** free warping and **b** restrained warping

parts of the loading machine in contact with them); (2) a second linear branch dominated by the axial stiffness of the specimen; and (3) a last softening phase corresponding to the post-buckling regime. The axial load corresponding to the ending of the linear stage (transition among phases 2 and 3) indicates the buckling load [12].

Actually, the transition between the second and the third phase is pretty gradual because of initial imperfections (i.e., no real bifurcation between a fundamental and a secondary branch may exist, see [17]), and a precise identification of the buckling load is not easy. Thus, the use of a second indicator results of help, as shown in Figs. 12b, 13b and 14b, where the curves of experimental axial load versus normalised torsion angle are shown. This angle may be taken as the kinematic parameter describing the apparent beam stiffness against torsion buckling. Its values were normalised with respect to the maximum values attained during each test, so to allow a direct comparison among the several tests. It is worth mentioning that, due to the initial geometrical imperfections, the twist rotation appears almost at once. The change in the sense of rotation recorded sometimes, especially after the initial settlement, can be ascribed to the combined effect of initial imperfections (of both geometry and loading) and of non-uniform local

plasticisation of the constrained regions, which defined the weakest rotation sense as the load was increased; see in particular cases 2 and 5 of Fig. 12b, case 6 of Fig. 13b.

The general responses in Figs. 12b, 13b and 14b reflect the three stages described above for the load–displacement curves. At the end of the second phase (i.e., at the end of the pre-critical branch), the twist angle starts increasing more rapidly with the load, thus exhibiting a softening response corresponding to the post-buckling regime [12].

Considering the material yield stress  $\sigma_y = 120$  MPa, the values of the elastic buckling pressure in Table 3 suggest that some inelastic behaviour took place, even though localised at a small portion of the profile, where the strains are more relevant. This inevitably implies that we must admit that buckling occurred in the elastic–plastic range, even though the beam is not fully plasticised. Accordingly, even the effective buckling load had to be evaluated in the elastic–plastic regime. To the purpose, Johnson’s parabolic formula was adopted [1, 12, 33]. This formula, dated back to 1893, works well for ductile metal columns and is still today the basis of the modern column design curves, as one can find in national and international codes of practice and recommendations [34]. Thus, the critical buckling load coincides either with the elastic buckling load  $N_{b,e} = \sigma_{b,e} A$  if  $\sigma_{b,e} \leq \sigma_y/2$ , or with the inelastic buckling load  $N_{b,ep} = \sigma_{b,ep} A$  otherwise, where  $A$  is the current cross-sectional area (see Table 2) and:

$$\sigma_{b,ep} = \sigma_y - \frac{\sigma_y^2}{4\sigma_{b,e}} \tag{1}$$

Table 8 shows the numerical inelastic buckling loads and the corresponding pressures provided by this empirical-theoretical approach, calculated by considering as ingredients of Johnson’s formula (1) the numerical outputs of the elastic buckling loads given by FEM (Table 3).

In Figs. 12, 13 and 14 red dashes, indicating the numerical value of the inelastic buckling load evaluated by Johnson’s empirical formula, are superimposed to the experimental curves. Despite the approximate and empirical nature of this formula, a very good agreement between experimental and FEM numerical results is found. In addition, we remark that in general the numerical predictions appear to be

**Fig. 12** Experimental curves for cases 1, 2, 4, 5 of Table 3 (one stiffener, free ends warping): **a** axial load versus axial displacement, **b** axial load versus normalised twist angle. Red dashes fix the numerical inelastic buckling loads

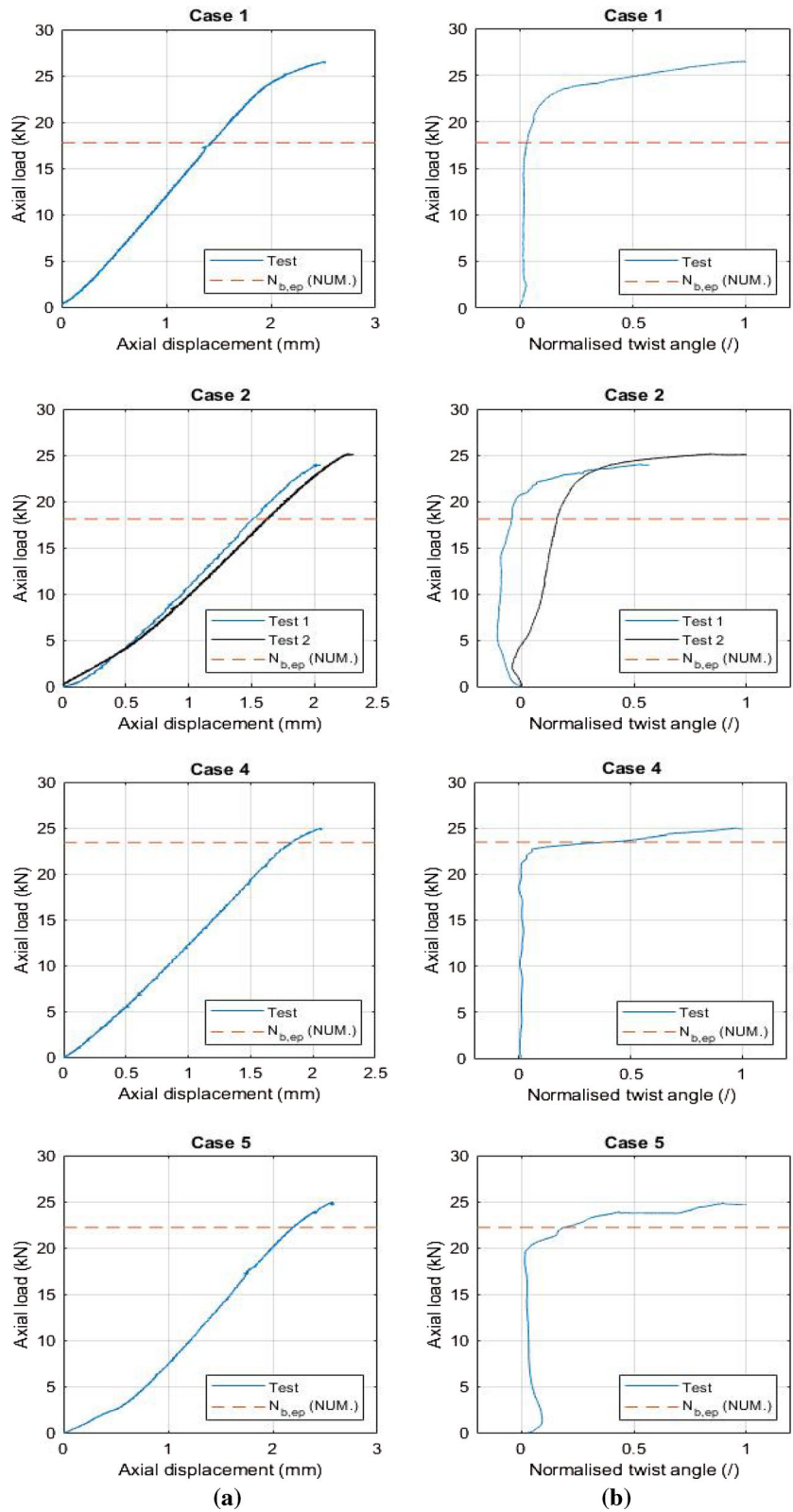
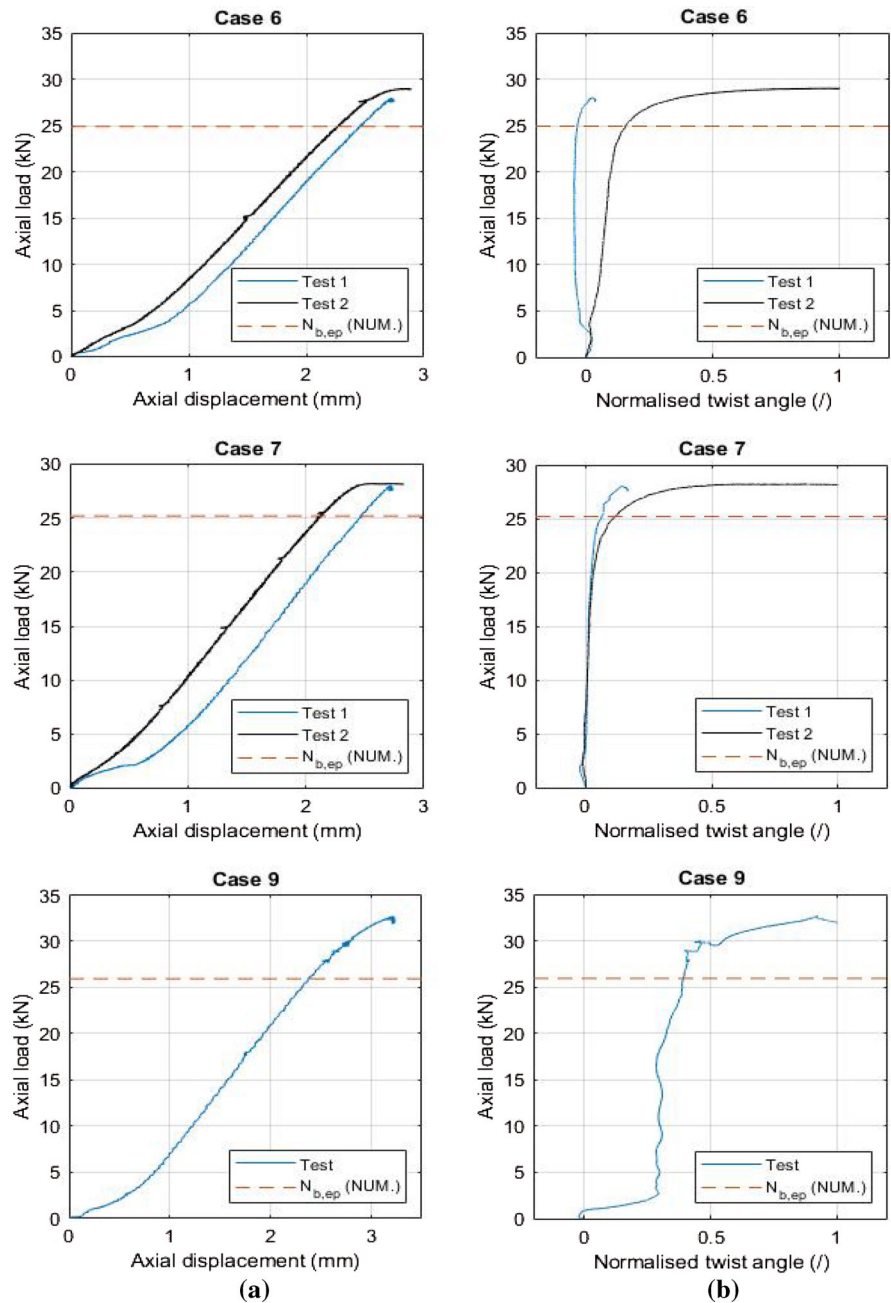




**Fig. 13** Experimental curves for cases 6, 7, 9 of Table 3 (one stiffener, restrained ends warping): **a** axial load versus axial displacement, **b** axial load versus normalised twist angle. Red dashes fix the numerical inelastic buckling loads



conservative; no need to stress the fact that such an indication is strongly in favour of technical design since it goes in favour of safety. This can be considered enough for the purpose of the present study, while a numerical modelling of inelastic torsion buckling of aluminium thin-walled profiles would go far beyond [20, 21, 35, 36].

### 6 Conclusions

Our *in-house* numerical code for the analysis of TWBs, relying on finite differences, is able to describe warping effects through a coarse one-dimensional beam model. It proved to be quick, efficient and reliable, but gave counterintuitive results (i.e., a decrease in the buckling load) when locally stiffened

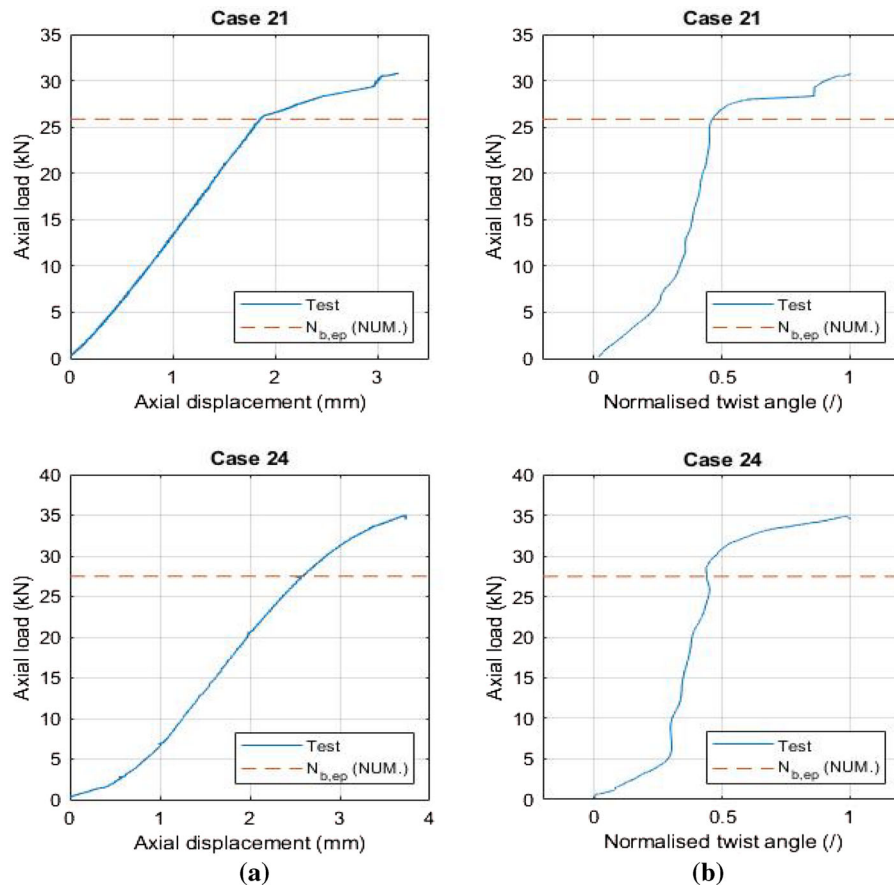


**Fig. 14** Experimental curves for cases 21 and 24 of Table 3 (two symmetric stiffeners): **a** axial load versus axial displacement, **b** axial load versus normalised twist angle. Red dashes fix the numerical inelastic buckling loads

profiles were considered. In this contribution we presented a thorough comparison of experimental and numerical results on the effect of local stiffeners on the buckling load capacity of multi-symmetric open thin-walled beams. The experimental campaign was performed on a series of specifically designed and manufactured aluminium specimens and stiffeners. These required a small amount of material and manufacturing but remarkable increased the buckling strength, which, however, is very sensitive to the placement of the stiffener, emphasizing the crucial role of a proper design. From this standpoint, the experimental and numerical results shown here are a benchmark for future developments.

The numerical analysis directly compared the results of a commercial code, where shell finite elements were used, with those of the *in-house* one, assuming a linearly elastic material. On the other hand,

the *in-house* code well catches the contributions of end constraints towards warping but gives unexpected results (if not properly interpreted) as for the intermediate stiffeners. In fact, warping constraints can be specified by imposing boundary conditions; the stiffening effect relies on the geometrical properties assigned to the cross sections of the reinforced chunks. Physical intuition and a careful examination of the FEM results suggested a different view of the stiffened beam chunk in both the one-dimensional theoretical and numerical models, i.e., as an inner warping constraint. In this way, the surprising results were overcome, and the FEM results were fully recovered. The numerical elastic buckling loads were thus used to calculate inelastic buckling loads, which matched well the experimental results.

From the satisfactory comparison of experimental and numerical results we thus believe that our present

**Table 8** Theoretical inelastic buckling loads and pressures for the cases of Table 3 experimentally tested

Case n.	Inelastic buckling load $N_{b,ep}$ (kN)	Inelastic buckling pressure $\sigma_{b,ep}$ (MPa)
1	17.77	70.57
2	18.07	71.75
4	23.49	93.26
5	22.26	88.38
6	24.95	99.08
7	25.19	100.03
9	25.93	102.96
21	25.86	102.68
24	27.51	109.24

contribution may serve as an indication towards design purposes, most of all since we proved that small amounts of material provide technically remarkable effects. At the same time, the interesting remark on the modelling of the local stiffeners opens new questions both from the theoretical and numerical points of view, which pave the way for further investigations that are in due course and will be reported elsewhere.

**Funding** Open access funding provided by Politecnico di Torino within the CRUI-CARE Agreement. The authors gratefully acknowledge the support of institutional grants (*Progetti di ricerca d'ateneo*) of the University “La Sapienza” (funding codes: RG11715C82466251, RG1181642C7528BF, RM11916B89334BE).

#### Declaration

**Conflict of interest** The authors declare that they have no conflict of interest.

**Open Access** This article is licensed under a Creative Commons Attribution 4.0 International License, which permits use, sharing, adaptation, distribution and reproduction in any medium or format, as long as you give appropriate credit to the original author(s) and the source, provide a link to the Creative Commons licence, and indicate if changes were made. The images or other third party material in this article are included in the article’s Creative Commons licence, unless indicated otherwise in a credit line to the material. If material is not included in the article’s Creative Commons licence and your intended use is not permitted by statutory regulation or exceeds the permitted use, you will need to obtain permission directly from the copyright holder. To view a copy of this licence, visit <http://creativecommons.org/licenses/by/4.0/>.

#### References

1. Timoshenko S, Gere JM (1961) Theory of elastic stability. McGraw-Hill, New York
2. Vlasov VZ (1963) Thin-walled elastic beams. Monson, Jerusalem
3. Piana G, Carpinteri A, Lofrano E, Malvano R, Manuello A, Ruta G (2016) Experimental and numerical elastodynamic analysis of compressed open thin-walled beams. In: Mains M (ed) Topics in modal analysis & testing, volume 10: proceedings of the 34th IMAC. Springer, pp 125–138
4. Piana G, Carpinteri A, Lofrano E, Ruta G (2017) Vibration and buckling of open TWBs with local weakening. *Procedia Eng* 199:242–247
5. Piana G, Lofrano E, Manuello A, Ruta G (2017) Natural frequencies and buckling of compressed non-symmetric thin-walled beams. *Thin Wall Struct* 111:189–196
6. Piana G, Lofrano E, Manuello A, Ruta G, Carpinteri A (2017) Compressive buckling for symmetric TWB with non-zero warping stiffness. *Eng Struct* 135:246–258
7. Woinowsky-Krieger S (1950) The effect of an axial force on the vibration of hinged bars. *J Appl Mech* 17:35–36
8. Bishop RED, Price WG (1974) The vibration characteristics of a beam with an axial force. *J Sound Vib* 59:237–244
9. Bokaian A (1988) Natural frequencies of beams under compressive axial loads. *J Sound Vib* 126:49–65
10. Bokaian A (1990) Natural frequencies of beams under tensile axial loads. *J Sound Vib* 142:481–498
11. Stephen NG (1989) Beam vibration under compressive axial load—upper and lower bound approximation. *J Sound Vib* 131:345–350
12. Bazant ZP, Cedolin L (1991) Stability of structures. Oxford University Press, New York
13. Rajkannu JS, Jayachandran SA (2020) Flexural-torsional buckling strength of thin-walled channel sections with warping restraint. *J Constr Steel Res* 169:106041
14. Lofrano E, Paolone A, Ruta G (2013) A numerical approach for the stability analysis of open thin-walled beams. *Mech Res Commun* 48:76–86
15. Ruta G, Varano V, Pignataro M, Rizzi N (2008) A beam model for the flexural-torsional buckling of thin-walled beams with some applications. *Thin-Wall Struct* 46:816–822

16. Pignataro M, Rizzi N, Ruta G, Varano V (2009) The effects of warping constraints on the buckling of thin-walled structures. *J Mech Mater Struct* 4:1711–1727
17. Pignataro M, Rizzi N, Luongo A (1991) Stability, bifurcation, and postcritical behaviour of elastic structures. Elsevier, Amsterdam
18. Hodges DH (2003) Geometrically exact, intrinsic theory for dynamics of curved and twisted anisotropic beams. *AIAA J* 41:1131–1137
19. Mølmann H (1982) Finite displacements of thin-walled beams 2—strain energy and variational principles. The Danish center for applied mathematics and mechanics, report no. 252
20. Battini J, Pacoste C (2002) Co-rotational beam elements with warping effects in instability problems. *Comput Method Appl M* 191(17–18):1755–1789
21. Duan L, Zhao J (2019) A geometrically exact cross-section deformable thin-walled beam finite element based on generalized beam theory. *Comput Struct* 218:32–59
22. Szewczak RM, Smith EA, DeWolf JT (1983) Beams with torsional stiffeners. *J Struct Eng* 109(7):1635–1647
23. Svensson SE, Plum CM (1983) Stiffener effects on torsional buckling of columns. *J Struct Eng* 109(3):758–772
24. Kreja I, Szymczak C (2002) Numerical simulation of a thin-walled beam with warping stiffeners undergoing torsion. *Task Q* 6(3):453–460
25. Kreja I, Szymczak C (2003) On numerical analysis of a thin-walled I-beam with warping stiffeners under torsional loads. In: CD-ROM. Burczyński T, Fedeliński P, Majchrzak E (eds) Computer methods in mechanics CMM-2003, Gliwice/Wisła, Poland, 3–6 June 2003, Gliwice, Silesian Technical University
26. Iwicki P (2010) Selected problems of stability of steel structures. Politechnika Gdańska, Gdańsk, ch. 3
27. Piana G, Lofrano E, Carpinteri A, Ruta G (2017) Buckling of an open thin-walled beam with an intermediate stiffener. In: Ascione L, Berardi V, Feo L, Fraternali F, Tralli AM (eds) AIMETA 2017—proceedings of the 23rd conference of the Italian association of theoretical and applied mechanics, vol 2, pp 800–807. ISBN 978-889-42484-7-0
28. Andraeus UA, Ruta G (1998) A review of the problem of the shear centre(s). *Cont Mech Thermodyn* 10:369–380
29. <http://www.lusas.com>
30. Szymczak C, Kujawa M (2017) Distortional buckling of thin-walled columns of closed quadratic cross-section. *Thin Wall Struct* 113:111–121
31. Brunetti M, Lofrano E, Paolone A, Ruta G (2015) Warping and Ljapounov stability of non-trivial equilibria of non-symmetric open thin-walled beams. *Thin Wall Struct* 86:73–82
32. Di Re P, Lofrano E, Addessi D, Paolone A (2020) Enhanced beam formulations with cross-section warping under large displacements. *Lecture Notes in Mechanical Engineering*. Springer, Cham, pp 1217–1229
33. Johnson JB, Bryan CW, Turneaure FE, Kinne WS (1916) The theory and practice of modern framed structures—designed for the use of schools and for engineers in professional practice, part III: design. Wiley, New York
34. Ziemian RD (ed) (2010) Guide to stability design criteria for metal structures, 6th edn. Wiley, New York
35. Guarracino F, Simonelli MG (2017) The torsional instability of a cruciform column in the plastic range: analysis of an old conundrum. *Thin Wall Struct* 113:273–286
36. Shamass R (2020) Plastic buckling paradox: an updated review. *Front Built Env* 6

**Publisher's Note** Springer Nature remains neutral with regard to jurisdictional claims in published maps and institutional affiliations.